ADVANCED FUNCTIONAL MATERIALS
www.afm-journal.de

Layer-by-Layer Assembly-Based Electrocatalytic Fibril Electrodes Enabling Extremely Low Overpotentials and Stable Operation at 1 A cm^{-2} in Water-Splitting Reaction

Younji Ko, Jinho Park, Jeongmin Mo, Seokmin Lee, Yongkwon Song, Yongmin Ko, Hoyoung Lee, Yongju Kim, June Huh, Seung Woo Lee, and Jinhan Cho**

For the practical use of water electrolyzers using non-noble metal catalysts, it is crucial to minimize the overpotentials for the hydrogen and oxygen evolution reactions. Here, cotton-based, highly porous electrocatalytic electrodes are introduced with extremely low overpotentials and fast reaction kinetics using metal nanoparticle assembly-driven electroplating. Hydrophobic metal nanoparticles are layer-by-layer assembled with small-molecule linkers onto cotton fibrils to form the conductive seeds for effective electroplating of non-noble metal electrocatalysts. This approach converts insulating cottons to highly electrocatalytic textiles while maintaining their intrinsic 3D porous structure with extremely large surface area without metal agglomerations. To prepare hydrogen evolution reaction (HER) and oxygen evolution reaction (OER) electrodes, Ni is first electroplated onto the conductive cotton textile (HER electrode), and NiFe is subsequently electroplated onto the Ni–electroplated textile (OER electrode). The resulting HER and OER electrodes exhibit remarkably low overpotentials of 12 mV at 10 mA cm^{-2} and 214 mV at 50 mA cm^{-2}, respectively. The two-electrode water electrolyzer exhibits a current density of 10 mA cm^{-2} at a low cell voltage of 1.39 V. Additionally, the operational stability of the device is well maintained even at an extremely high current density of 1 A cm^{-2} for at least 100 h.

1. Introduction

Hydrogen (H_2) is the cleanest fuel available and has the potential to meet the energy needs of future societies owing to its high energy density and energy conversion efficiency.[1] However, at present, it has been generated from chemical processes that are based on fossil fuels (i.e., steam methane reforming and coal gasification), resulting in the production of large amounts of carbon dioxide.[2] Therefore, electrocatalytic splitting of water into hydrogen (i.e., the hydrogen evolution reaction; HER) at the cathode and oxygen (i.e., the oxygen evolution reaction; OER) at the anode has been recognized as a promising alternative to the current fossil fuel-based hydrogen energy system.[3,4] Considerable research efforts have been devoted to developing efficient and low-cost HER and OER electrocatalysts composed of non-noble metal composites (mainly binary metal composites based on Ni, Co, Fe, Mo, and/or W) to replace noble and rare metal (Pt, Ir, and Ru)-based electrocatalysts.[5–9] These electrocatalysts have been mainly deposited onto porous metal foams or conductive carbon substrates with the relatively large surface area for the preparation of HER and OER electrodes.[10–13] Several different approaches have been also made to overcome the intrinsically low activity of non-noble metal catalysts. These approaches include controlling the chemical composition, synthesizing high-index faceted catalysts, and increasing the specific surface area.[8,14] Despite some progress, the performance of non-noble metal electrocatalyst-based systems remains well below that of their noble-metal counterparts.

Y. Ko, J. Mo, S. Lee, Y. Song, Prof. J. Huh, Prof. J. Cho
Department of Chemical & Biological Engineering
Korea University
145 Anam-ro, Seongbuk-gu, Seoul 02841, Republic of Korea
E-mail: jinhan71@korea.ac.kr

Dr. J. Park, H. Lee, Prof. S. W. Lee
G. W. Woodruff School of Mechanical Engineering
Georgia Institute of Technology
Atlanta, GA 30332-0245, USA
E-mail: seung.lee@me.gatech.edu

The ORCID identification number(s) for the author(s) of this article can be found under https://doi.org/10.1002/adfm.202102530.

DOI: 10.1002/adfm.202102530

Dr. J. Park
Aerospace, Transportation and Advanced Systems Laboratory
Georgia Tech Research Institute
Georgia Institute of Technology Atlanta
Atlanta, GA 30332, USA

Dr. Y. Ko
Division of Energy Technology
Materials Research Institute
Daegu Gyeongbuk Institute of Science and Technology (DGIST)
333 Techno Jungang-daero, Hyeonpung-eup, Dalseong-gun,
Daegu 42988, Republic of Korea

Prof. Y. Kim, Prof. J. Cho
KU-KIST Graduate School of Converging Science and Technology
Korea University
145 Anam-ro, Seongbuk-gu, Seoul 02841, Republic of Korea

Recently, paper and cotton substrates composed of cellulose fibrils have emerged as multifunctional substrates for energy storage and conversion devices, with advantages including their low cost, high surface areas, and 3D porous structures.[16] For these electrochemical applications including water-splitting, depositing electrically conductive and electrochemically active materials on these substrates is essential for overcoming their insulating property. Furthermore, conformal deposition of the conductive and active materials over the entire porous substrates (from the outermost to central regions) is critical for the effective utilization of their large surface area and achieving high electrochemical performance. To achieve this goal, various deposition processes, such as painting, sputtering, and electroless (EL) deposition (i.e., chemical reduction deposition), have been used to incorporate conductive and catalytic materials into these 3D paper or cotton substrates.[16] However, these deposition processes have much difficulty in inducing highly uniform coating and structures due to inadequate control of the interfacial interactions between the substrate and the introduced conductive, catalytic components. Furthermore, these phenomena can limit the overall conductivity and catalytic activity for water-splitting. To our knowledge, the overpotentials for most non-noble metal textile-based electrodes except porous metal-based electrodes have exceeded 30 and 270 mV for the HER and the OER, respectively (at 10 mA cm^{-2}).

Herein, we introduce an electrocatalytic fibril-based water-splitting electrode fabricated by a layer-by-layer (LbL)-assembled metal nanoparticle (NP)-induced electroplating. For this study, tetra(octyl ammonium) (TOA)-stabilized metal NPs, which were used as conductive seeds for the model system, were conformally and successively coated onto amine (NH_2)-modified cotton fibrils using a unique ligand-exchange-based LbL-assembly between bulky TOA ligands and small molecule linkers, which resulted in sufficient electrical conductivity for subsequent electrocatalytic (Ni and NiFe) electroplating. Although TOA-Au NPs were preferentially used as a conductive metal component in our study, it should be noted that other metal NPs such as TOA-Cu NPs and TOA-Ag NPs showing a high affinity with NH_2-modified cotton can be also employed as conductive seeds instead of Au NPs (a more detailed explanation and evidences are given in the latter part). In this case, the metal NPs are easily incorporated into the cotton textiles owing to the high affinity (i.e., covalent bonding) between the amine (NH_2)-modified cotton fibrils and the surface of the metal NPs. They can also be uniformly and densely deposited onto all the regions from the exterior to the interior of the textile, maintaining its porous structure. Particularly, we highlight that this LbL-assembled metal NPs using small molecule linkers is required for the preparation of conductive textile (10^2–10^3 Ω sq^{-1}) that is suitable for robust and uniform Ni electroplating. It should also be noted that this conductive textile cannot be easily realized by conventional electrostatic LbL-assembly between charged metal NPs and oppositely charged polymer linkers in aqueous solution.[17–19] Additionally, our research goals are to lower the overpotentials for HER and OER using large surface area of LbL-assembly-induced metallic cotton fibrils, and simultaneously enhance the mechanical flexibility and operation stability using favorable interfacial interactions between textiles and electrocatalytic components. In addition, Ni and NiFe electroplating onto the metal NP-assembled cotton textiles led to an extremely low sheet resistance (<0.1 Ω sq^{-1}).

Furthermore, our approach produced a large amount of highly active β-$Ni(OH)_2$ (particularly compared to that of α-$Ni(OH)_2$ showing relatively low HER performance) and NiFe layered double hydroxide (NiFe LDH) with a nanosized protuberant and wrinkled structure that enhanced the HER and the OER performances, respectively. The highly conductive 3D porous network structure of β-$Ni(OH)_2$ and NiFe LDH increases the active surface area of electrodes, and also facilitates charge and mass transport. When the Ni– and NiFe–cotton electrodes were applied to the HER and OER, respectively, they exhibited low overpotentials of 12 mV (for the HER at 10 mA cm^{-2}) and 214 mV (for the OER at 50 mA cm^{-2}), and also maintained the stable operation (>at least 100 h) at an extremely high current density of 1 A cm^{-2} in 1 M KOH, exceeding the electrocatalytic performances of conventional non-noble metal-based textile electrodes. Considering that our approach could easily impart electrical and electrocatalytic properties to other insulating substrates, we believe that it is very effective in preparing a variety of other electrochemical electrodes as well as water-splitting electrodes that require a large active surface area and facile charge transfer.

2. Results and Discussion

2.1. Metal Electroplating Using LbL-Assembled Metal NPs

To fabricate our water-splitting electrodes (**Figure 1**), we first investigated the adsorption behavior of metal NPs using LbL-assembly based on the mutual interactions between two different components. TOA-Au NPs with a diameter of ≈7 nm in toluene were alternately LbL-assembled with small diethylenetriamine (DETA) molecules (M_w ≈103 g mol^{-1}) in ethanol onto Si substrates (**Figure 2**a,b). During LbL deposition, the amine groups (NH_2 and NH groups) of the DETA linkers were directly deposited onto the bare surfaces of the Au NPs via a ligand-exchange reaction between the bulky TOA ligands, which were loosely bound to the surfaces of the Au NPs, and DETA, which has a higher affinity for Au.

The presence of residual TOA ligands in the (TOA-Au NP/DETA)$_n$ multilayers was examined using Fourier transform infrared (FTIR) spectroscopy (Figure 2b and Figure S1, Supporting Information). The FTIR spectra of the TOA-Au NPs exhibited absorption peaks originating from the C–H stretching of the long alkyl chains of the TOA ligands at 2920 and 2860 cm^{-1} (i.e., n = 0.5 bilayers). However, as the extremely thin DETA layer was adsorbed onto the TOA-Au NP-coated substrate (n = 1.0 bilayers), the C–H stretching absorption peak almost completely disappeared. Therefore, the alternating deposition of the TOA-Au NPs and DETA produced inversely correlated changes in the peak intensities at the C–H stretching frequencies. This result indicates that the Au NP layers (e.g., 1.0- and 2.0-bilayer films) sandwiched between adjacent DETA layers did not contain bulky TOA ligands, which minimizes the separation distance (i.e., contact resistance) between neighboring Au NPs. Additionally, it should be noted that it is difficult for conventional

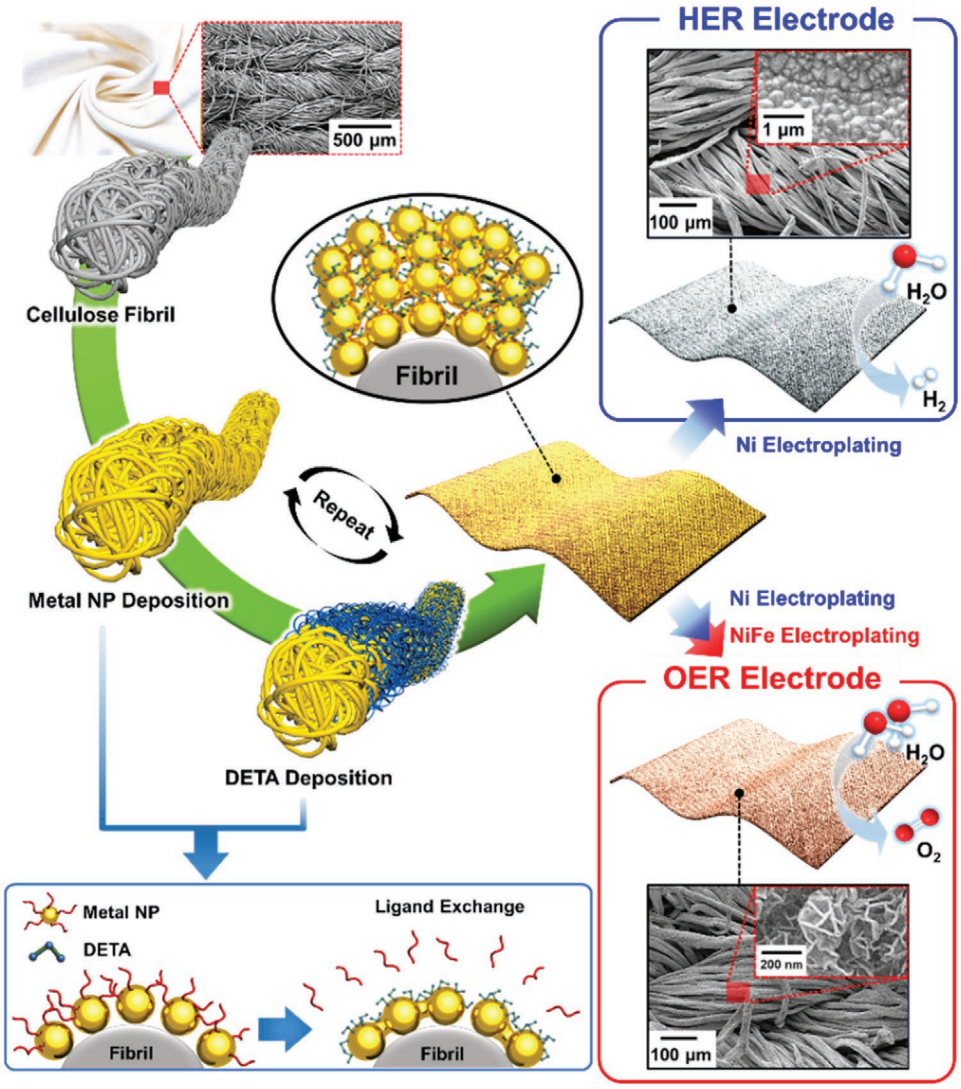

Figure 1. Schematic illustration of the conductive cotton for water-splitting electrocatalysts based on the metal NP assembly-driven electroplating approach.

electrostatic LbL-assembly using anionic Au NPs and cationic polymer linkers to prepare conductive textiles because the use of bulky polymer linkers and the strong electrostatic repulsion between neighboring Au NPs with the same negative charges significantly increase the contact resistances.[20]

The thickness per bilayer was measured to be ≈3.4 nm (Figure S2, Supporting Information), and the size of the Au NPs measured for (TOA-Au NP/DETA)$_{10}$ was much larger than that for the 1-bilayer film (or the as-synthesized Au NPs shown in Figure 2a), as shown in field emission-scanning electron microscopy (FE-SEM) images (Figure 2c). This implies that the dense packing of Au NPs during assembly induces partial metallic sintering of Au–Au NPs. Korgel et al. reported that metallic bonding can occur between metal NPs with low cohesive energy when the separation distance between neighboring metal NPs is less than 5 Å.[21]

To gain molecular-level insight into the interparticle distance of assembled Au NPs, we used atomistic molecular dynamics (MD) simulations of model systems for DETA between adjacent Au layers (Figure 2d). When it was considered that the Au NPs were almost perfectly covered by a DETA monolayer with a flat conformation (i.e., the ratio of the surface area covered by adsorbed DETA linkers to that covered by adsorbed Au NPs (S_{DETA}/S_{Au}) ≈ 1.0), the interparticle distance was estimated to be ≈5.4–6.7 Å. This minimized separation gap between neighboring Au NPs with low cohesive energy (3.81 eV per atom) can facilitate mutual atom diffusion within the LbL-assembled Au NPs, which can enhance the electrical conductivity.[20]

After testing the LbL-assembly method on the Si substrate, we then applied it to highly porous textiles composed of cotton fibrils (i.e., OH-functionalized cellulose fibrils) with widths of ≈23 μm. First, the surfaces of the cotton fibrils were amine-functionalized by poly(ethylene imine) (PEI) through hydrogen bonding interactions between the NH_2 groups of PEI and the OH groups of cotton fibrils. Then, TOA-Au NPs

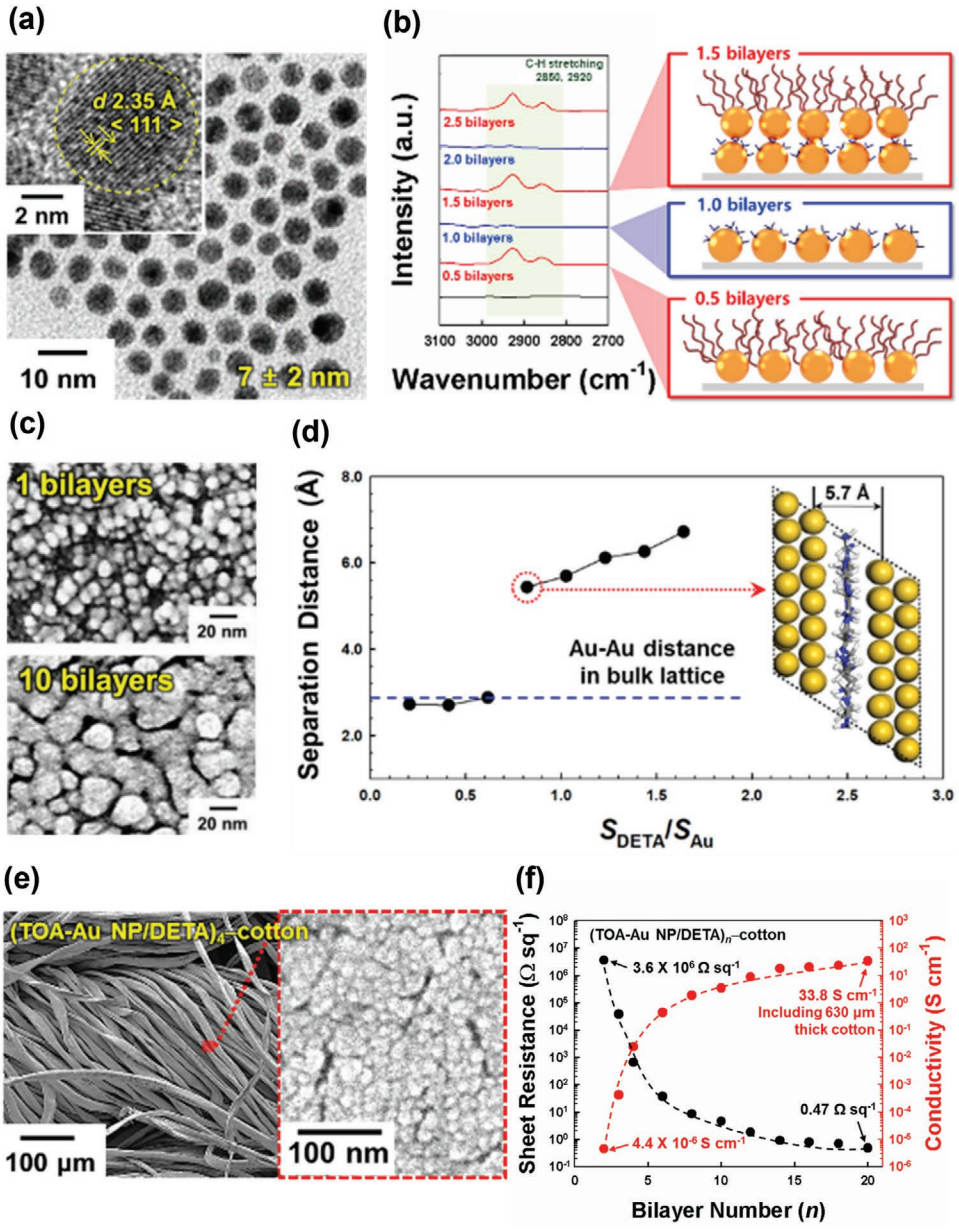

Figure 2. a) High-resolution transmission electron microscopy (HR-TEM) image of TOA-Au NPs dispersed in toluene. b) FTIR spectra and schematic representation of ligand-exchange reaction-induced LbL-assembled (TOA-Au NP/DETA)$_n$ multilayers as a function of bilayer number (n). c) Planar FE-SEM images of (TOA-Au NP/DETA)$_1$ and (TOA-Au NP/DETA)$_{10}$ multilayers. d) The MD-computed minimal distance between Au atomic surfaces separated by DETA molecules as a function of surface coverage ratio (S_{DETA}/S_{Au}). The blue dotted horizontal line shows the inter-particle distance of Au–Au in the bulk lattice (2.884 Å). The image in the r.h.s. represents the MD-simulated molecular structure of DETAs between Au atomic surfaces at S_{DETA}/S_{Au} = 1.0. e) Planar FE-SEM image of (TOA-Au NP/DETA)$_4$-coated cotton electrodes. f) Electrical properties of (TOA-Au NP/DETA)$_n$-coated cotton electrodes with increasing bilayer number.

were deposited onto PEI-coated cotton via the abovementioned ligand-exchange reaction. After this stable adsorption of TOA-Au NPs, DETA and TOA-Au NPs were alternately deposited onto the PEI-coated cotton substrates. Notably, the TOA-Au NP multilayers were uniformly and densely deposited on the surfaces of fibrils, infiltrating deeply without any NP agglomeration (Figure 2e and Figure S3, Supporting Information), although the first deposition of the TOA-Au NP layer (i.e., (TOA-Au NP/DETA)$_{n=1}$) exhibited insufficient surface coverage (Figure S4, Supporting Information). With increasing bilayer number (n) of the (TOA-Au NP/DETA)$_n$ multilayers from 1 to 20, the sheet resistance of the multilayer-coated textiles sharply decreased from 3.6×10^6 to 0.47 Ω sq^{-1}, and the electrical conductivity (including the thickness of the 630 μm-thick cotton textile) increased from 4.4×10^{-6} to 33.8 S cm^{-1} without any thermal or mechanical treatment (Figure 2f).

To prepare the water-splitting electrode, Ni was electroplated on the (TOA-Au NP/DETA)$_4$-deposited cotton textile with a

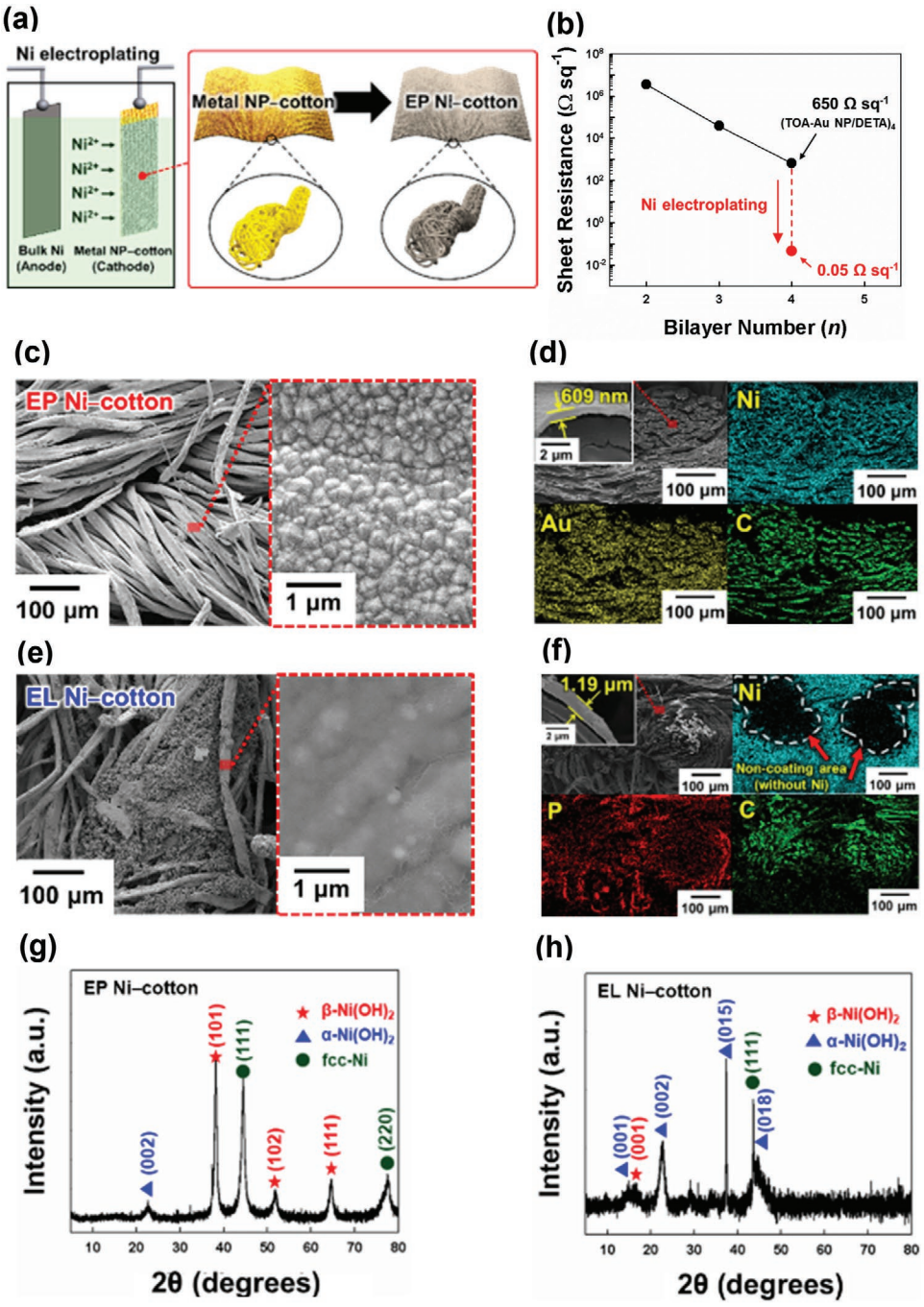

Figure 3. a) Schematic of the HER electrode fabricated using metal NP assembly-driven Ni electroplating deposition. b) Electrical properties of electroplated Ni-coated cotton (EP Ni–cotton). c) Planar FE-SEM images and d) cross-sectional energy-dispersive X-ray spectroscopy (EDX) mapping image of the EP Ni–cotton electrode (the top left inset shows the thickness of the EP Ni layer). e) Planar FE-SEM images and f) cross-sectional EDX mapping image of the EL Ni–cotton electrode (the top left inset shows the thickness of the EL Ni layer). XRD spectra of g) the EP Ni–cotton electrode and h) EL Ni–cotton electrode.

sheet resistance of ≈650 Ω sq^{-1} (**Figure 3**a,b). In this case, the loading amount of (TOA-Au NP/DETA)$_4$ multilayers adsorbed onto cotton substrate was measured to be ≈2.47 mg cm^{-2} (Note: TOA ligands are replaced by DETA, and additionally the M_w (103 g mol^{-1}) of DETA is similar to that (92 g mol^{-1}) of toluene solvent). Therefore, we assume that the loading mass of (TOA-Au NP/DETA)$_4$ is almost similar to that of Au NPs. Although a higher number of bilayers would have generally provided higher electrical conductivity suitable for the electroplating process, we selected (TOA-Au NP/DETA)$_4$-coated cotton, which had the minimum conductivity required, considering the process and time efficiency. When the (TOA-Au NP/DETA)$_4$-coated

cotton was electroplated (EP) at a current density of 346 mA cm^{-2} for 30 min, the thickness and loading mass of the EP Ni layer were measured to be ≈609 nm and 52 mg cm^{-2}, respectively. In addition, the thickness of the Ni layer can be controlled by the electroplating time (see Figure S5 in the Supporting Information).

The sheet resistance of the EP Ni-deposited cotton textile (i.e., EP Ni–cotton) decreased to 0.05 Ω sq^{-1} (Figure 3b), which was much lower than that (≈3 Ω sq^{-1}) of Ni–cotton textiles prepared using the EL Ni deposition process (i.e., chemical reduction of Ni precursors). In addition, the LbL-assembled Au NP layer used for the conductive seed was completely embedded beneath the 609 nm-thick EP Ni layer, which had no effect on electrocatalytic activities. We also confirmed that the resultant EP Ni–cotton could maintain low sheet resistance during 5000 cycles of repetitive mechanical bending tests, which implied the high mechanical flexibility and electrical stability of EP Ni–cotton (Figure S6, Supporting Information).

Importantly, the EP Ni components were uniformly coated onto all cotton fibrils from the outer surface to the central region of the cotton textiles without metal agglomeration. The EP Ni layer exhibited a highly protuberant surface morphology with a size of a few hundred nanometers (Figure 3c,d). As mentioned earlier, the deposition of a 609 nm-thick EP Ni layer onto conductive textiles implies that the electrical and electrocatalytic properties of EP Ni-cotton are completely governed by those of the EP Ni layer irrespective of the kind of conductive seeds (i.e., metal NPs) and textiles. By contrast, nonuniform coating areas (without Ni components) and partial aggregation of the Ni components were observed when applying the EL Ni deposition approach (Figure 3e,f).

Specifically, in the case of EL Ni deposition, Ni precursor ions are first deposited onto NH_2-functionalized cotton textiles and then chemically reduced with the aid of a reducing agent. However, it is worth noting that the Ni cationic ions are not densely adsorbed onto the cotton textiles during the first deposition step due to the long-range electrostatic repulsion between the Ni ions with the same charge. Additionally, when Ni seeds with low packing density are formed by chemical reduction, Ni ions are continuously incorporated into the seeds. As a result, the seeds concentrically grow onto the selected area through nucleation growth, which induces nonuniform Ni deposition onto the cotton textiles.

Therefore, the EL Ni layer was not evenly coated on the fibrils, so the thickness was not uniform on the inside and outside. Furthermore, this chemical reduction method has much difficulty in minutely controlling the coating process due to the complex process variables, including the metal precursor concentration, reducing agent concentration, and/or reaction time. As already mentioned above (see Figure S4, Supporting Information), this insufficient surface coverage could also be observed with the (TOA-Au NP/DETA)$_1$-coated cotton. However, our LbL-assembly approach using a multilayer structure could easily increase the surface coverage of conductive Au NPs onto cotton textiles, which resulted in the formation of a highly uniform electroplated Ni layer onto cotton textiles.

Although EL Ni was performed on (TOA-Au NP/DETA)$_4$-coated cotton with the outermost DETA layer, the surface morphology and electrical properties (≈3 Ω sq^{-1}) of the resultant EL Ni–cotton were similar to those of EL Ni–cotton without (TOA-Au NP/DETA)$_4$ multilayers (Figure S7, Supporting Information). It should be noted here that the electrical properties of EL Ni–cotton were entirely governed by the EL Ni layer (≈3 Ω sq^{-1}) instead of TOA-Au NP multilayers (≈650 Ω sq^{-1}). That is, the stable adsorption and electrical properties of the EL Ni layer strongly depend on the interfacial interaction between Ni precursor ions and the NH_2-functionalized surface of cotton substrates irrespective of the presence of Au NP multilayers. The specific surface areas of EL Ni–cotton and EP Ni–cotton, which were measured using Brunauer-Emmett-Teller (BET) analyzer, were ≈0.469 and 0.869 m^2 g^{-1}, respectively (Figure S8, Supporting Information). That is, the specific surface area of EP Ni–cotton was 2-fold higher relative to the EL Ni–cotton, which was 1.5 times higher than the bare cotton (0.581 m^2 g^{-1}), and on the other hand 0.65 times lower than the Au NP coated–cotton (1.347 m^2 g^{-1}), respectively.

As mentioned earlier, this increase in the specific surface of EP Ni–cotton was attributed to the large amount of Ni protrusions created during electroplating. These results also demonstrate that the metal NP assembly-driven electroplating approach can be effectively applied to the preparation of metal-like conductive and highly electrocatalytic cotton textiles while preserving their pristine porous structure with a large surface area. Furthermore, it should be noted that TOA-Ag NPs and TOA-Cu NPs can also be deposited with small amine linkers onto cotton textiles using the same ligand-exchange reaction-based LbL-assembly (a more detailed explanation will be given later and in the Supporting Information).

We also investigated the crystal structure of the EP Ni layer using X-ray diffraction (XRD) analysis. The XRD pattern of EP Ni mainly exhibited the characteristic (101), (102), and (111) reflection peaks assigned to β-$Ni(OH)_2$. Additionally, the (111) and (220) peaks of face-centered cubic (fcc) Ni and the minor (002) peak of α-$Ni(OH)_2$ were observed (Figure 3g). By contrast, the XRD pattern of the EL Ni layer exhibited the characteristic (001), (002), (015), and (018) peaks of α-$Ni(OH)_2$ and the (111) peak of fcc Ni (Figure 3h).[22] In addition, a negligible (001) reflection peak associated with β-$Ni(OH)_2$ was observed, confirming the dominant structure of α-$Ni(OH)_2$ in the EL Ni layer. Thus, unlike EL deposition, metal NP assembly-driven electroplating generates a large amount of β-$Ni(OH)_2$, which is known to be more active toward the HER.

Moreover, for Ni deposition through electroplating with the high reduction power of Ni ions, the crystalline structure was similar to that of the bulk Ni foam (mainly β-$Ni(OH)_2$ and fcc Ni) (Figure 3g and Figure S9, Supporting Information). However, EL Ni deposition strongly induces the formation of α-$Ni(OH)_2$ structures with a metastable phase rather than β-$Ni(OH)_2$ with a thermodynamically stable phase and a well-defined crystalline structure because of the relatively low reduction power and the formation of large amounts of impurities resulting from this chemical reduction approach (Figure 3h).[23–25] It was also reported by Hall et al. that EL Ni deposition or Ni electroplating using an external deposition current on the order of a few mA cm^{-2} mainly results in the formation of α-$Ni(OH)_2$, and electroplating using larger currents yields mixed α/β-phase materials.[26] In addition, they

reported that the structure (phase, crystallinity, and shape) of the nickel oxides is also dependent on the nature of the nickel salt solution (concentration and counter-ions). Therefore, considering that our EP Ni cotton substrates were prepared using a relatively high current density of 346 mA cm^{-2}, it is obvious that the phase materials formed by high-current-based Ni electroplating are different from those obtained by EL Ni deposition.

We further analyzed the NiO and $Ni(OH)_2$ in the EP Ni– and EL Ni–cotton textiles using X-ray photoelectron spectroscopy (XPS) (Figure S10, Supporting Information). The binding energies of EP Ni–cotton were negatively shifted by 0.1–0.3 eV relative to those of EL Ni–cotton, which indicates the formation of weaker Ni–OH bonds (i.e., longer Ni–O bonds) in the β-$Ni(OH)_2$ of the EP Ni layer than in the EL Ni–deposited layer. Thus, considering that weaker Ni–OH bonds have stronger hydrogen bonding interactions with water molecules in alkaline media, the EP Ni layer can enhance HER activity compared with the EL Ni layer that has relatively strong Ni–OH bonds in $Ni(OH)_2$.[27]

Recently, α-$Ni(OH)_2$ was reported to have a larger interlayer distance (0.70–0.90 nm) than β-$Ni(OH)_2$ (0.46–0.48 nm) due to the presence of interlamellar water molecules and/or impurities in the α-$Ni(OH)_2$ lattice.[28] Additionally, the researchers demonstrated that the hydrogen bonding between interlamellar water molecules and the lamellar hydroxyl groups of α-$Ni(OH)_2$ decreases HER activity because the adsorbed water molecules and/or impurities cannot act as HER reactants. These results support our conclusion that β-$Ni(OH)_2$ without internal water molecules has higher activity in the HER than α-$Ni(OH)_2$.

2.2. HER Textile Electrode Using Electroplated Ni

We confirmed the exceptional HER performance of the EP Ni–cotton textile in a three-electrode electrochemical cell using 1 M KOH electrolyte, which was in stark contrast with the performance of commercial Ni foam and the EL Ni–cotton textile (**Figure 4**a). The high HER activity of EP Ni–cotton was not attributed to the electrocatalytic activity of the Au NP layer buried below the Ni layer (Figure S11, Supporting Information). It should also be noted that the $(TOA\text{-}Au\ NP/DETA)_4$ multilayers with a thickness of ≈13 nm and a relatively high sheet resistance of ≈650 Ω sq^{-1} provide only the minimal electrical conductivity for the formation of a uniform Ni layer during the electroplating process. Therefore, the formed EP Ni–cotton exhibited an electrical conductivity of ≈0.05 Ω sq^{-1}, which was superior to that of the EL Ni–cotton (≈3 Ω sq^{-1}). These phenomena evidently demonstrate that the EP Ni layer on the $(TOA\text{-}Au\ NP/DETA)_4$–cotton fully governs the electrical conductivity, the active surface area, and the resultant HER performance.

The EP Ni–cotton electrode exhibited overpotentials of 12 and 59 mV at current densities of 10 and 50 mA cm^{-2} for the HER, respectively, which were much lower than that of the EL Ni–cotton electrode (89 mV at 10 mA cm^{-2}). Additionally, we confirmed that when the potential increases from –0.025 to –0.175 V, the activity difference between EP Ni– and EL Ni–cotton electrodes was slightly decreased. Specifically, The EP Ni–cotton electrode displayed the current densities of 22.4 and 320.2 mA cm^{-2} at the potentials of –0.025 and –0.175 V, respectively, which were ≈8.3 and 6.3 times higher than that of the EL Ni–cotton electrode, respectively (Figure S12, Supporting Information). Although the HER performance of EL Ni–cotton with the $(TOA\text{-}Au\ NP/DETA)_4$ multilayers (i.e., EL Ni–Au–cotton) was slightly improved compared to that of EL Ni–cotton without $(TOA\text{-}Au\ NP/DETA)_4$ presumably due to the slight change in the active surface area of the EL Ni layer (Figures S13 and S14, Supporting Information), its performance (i.e., overpotentials ≈40 and 138 mV at 10 and 50 mA cm^{-2}, respectively) was still substantially inferior to that (i.e., overpotentials of 12 and 59 mV at 10 and 50 mA cm^{-2}) of EP Ni–cotton.

To further demonstrate the effect of the EP Ni layer on HER performance, we also prepared samples on a flat substrate and then measured their HER for a relative performance comparison, i.e., 1) an EP Ni/Au sputtered-flat Si substrate (EP Ni–flat wafer) and 2) an EL Ni/Au sputtered-flat Si substrate (EL Ni–flat wafer). The flat substrate used for these samples could minimize the effect of the macroporous structure of cotton substrates on HER performance, although the EP Ni–flat wafer also has nanosized protuberances that influence the active surface area (Figure S15, Supporting Information). In this case, the HER performance of the EP Ni–flat wafer outperformed that of the EL Ni–flat wafer (Figure S16, Supporting Information), which coincided with the performance trend between the EP Ni–cotton and the EL Ni–cotton to some degree. Compared to the nonporous and flat substrate, the cotton substrate induced the onset potential shift, which implied the enhanced water dissociation performance occurring from an increase of the β-$Ni(OH)_2$ surface (provided by the 3D porous structure per geometrical surface area). Additionally, when the Ni electroplating process was applied to a flat Ni plate instead of a gold-coated Si wafer, a protuberant nanostructure in the EP Ni–flat wafer was also formed (Figure S17a, Supporting Information), and the resulting HER performance was similar to that of the EP Ni–flat wafer under the same experimental conditions (Figure S17b, Supporting Information). These results demonstrate that the remarkably low overpotential of EP Ni–cotton is mainly caused by the structural uniqueness (i.e., crystal structure and protuberant nanostructure) of the EP Ni layer as well as the large surface area of cotton electrodes with high electrical conductivity. Furthermore, these results imply that the HER performance of EP Ni–cotton is entirely governed by the EP Ni layer irrespective of TOA-Au NP/DETA multilayers.

The catalytic activity of electrocatalysts strongly depends on the electrochemically active surface area (ECSA). To estimate the ECSA, we measured the electric double-layer capacitance of EP Ni–cotton and EL Ni–cotton using scan-rate-dependent cyclic voltammetry in 1 M KOH (Figure S18, Supporting Information).[28] With a specific capacitance of 0.040 mF cm^{-2} of Ni,[7] the ECSA of the EP Ni–cotton electrode was calculated to be ≈1835 cm^2, which was 1.3 times higher than that of the EL Ni–cotton electrode (1387.5 cm^2). To evaluate the intrinsic activity of the Ni electrocatalysts, the current densities were normalized with respect to the ECSA. In this case, the EP Ni–cotton exhibited

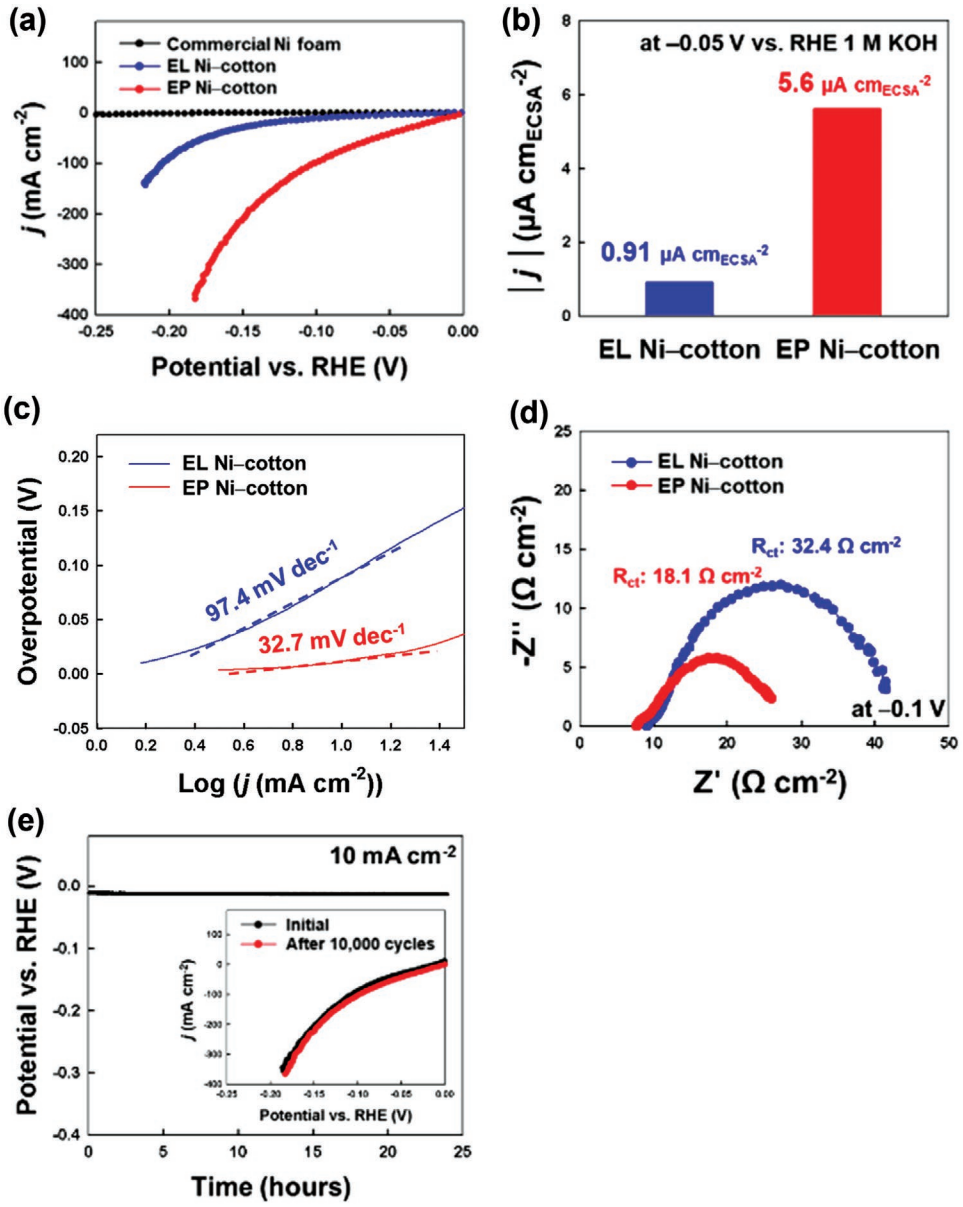

Figure 4. a) HER polarization curves recorded with Ni foam, EL Ni–cotton, and EP Ni–cotton electrodes in a 1 M KOH electrolyte at a scan rate of 10 mV s^{-1}. Herein, j is defined as geometrical areal current density. b) Intrinsic HER activity (μA cm^{-2}_{ECSA}) of EL Ni– and EP Ni–cotton electrodes normalized with respect to the ECSAs of the electrocatalysts. In this case, $|j|$ is defined as absolute value of the current density normalized with respect to the ECSAs. c) Tafel plots for the EL Ni–cotton and EP Ni–cotton electrodes. d) EIS plots for the EL Ni–cotton and EP Ni–cotton electrodes at an applied potential of –0.1 V (vs RHE). e) Chronopotentiometric stability test of the EP Ni–cotton electrode at 10 mA cm^{-2}. The inset shows the polarization curves recorded before and after 10 000 cycles of potential sweeps in the range of +0.02 to –0.4 V (vs RHE).

an approximately sixfold enhancement in intrinsic activity relative to the EL Ni–cotton at –0.05 V versus a reversible hydrogen electrode (RHE) (Figure 4b). Therefore, it is reasonable to conclude that the enhanced intrinsic activity of the EP Ni–cotton electrode is mainly caused by the aforementioned favorable crystalline structure and binding energies. The high active surface area of the formed nickel hydroxides significantly contributes to the high HER performance of EP Ni–cotton. Another benefit of our EP Ni–cotton electrode is its fast kinetics. Specifically, the Tafel slope of EP Ni–cotton electrode (i.e., HER electrode) was ≈32.7 mV dec^{-1}, indicating that the Tafel step operates as a rate-limiting step for HER in EP Ni–cotton electrode.[7,28–31] The lower Tafel slope of EP Ni–cotton electrode than that of EL Ni–cotton electrode (97.4 mV dec^{-1}) also implies the higher efficiency of water dissociation (Figure 4c).

We also confirmed the fast kinetics using electrochemical impedance spectroscopy (EIS) (Figure 4d). The EP Ni–cotton exhibited much lower charge transfer resistance (R_{ct}) of 18.1 Ω cm^{-2} than that of the EL Ni–cotton (R_{ct} ≈32.4 Ω cm^{-2}), which is indicative of more efficient electron transfer between the electrode surface and electrolyte.[31] In addition, the lower equivalent series resistance of EP Ni–cotton (R_s ≈7.9 Ω cm^{-2} at

100 kHz) than that of EL Ni–cotton (R_s ≈9.1 Ω cm^{-2} at 100 kHz) means that EP Ni–cotton was more electrically conductive than EL Ni–cotton, which contained a relatively large amount of impurities, as mentioned earlier. The HER performance of our EP Ni–cotton textiles (Tafel slope and overpotential) was superior to those of Ni nanocomposites with mixed metal components (e.g., NiFe(oxo) hydroxide/Ni, NiS/Ni, FeP/Ni_2P/Ni, and NiMo/Ni)[10–12,12,33–39] reported to date (Table S1, Supporting Information). Furthermore, our electrodes could stably maintain high electrocatalytic activity without notable structural or morphological changes in the EP Ni (Figure 4e and Figures S19 and S20, Supporting Information).

2.3. OER Textile Electrode Using Electroplated NiFe

Even with exceptional performance for the HER, the overall kinetics of the electrochemical water-splitting process can be significantly hindered by a sluggish anodic OER. To obtain a high-performance, non-noble OER catalyst, we carried out an additional electroplating step to deposit NiFe onto the highly conductive EP Ni–cotton textile. We selected NiFe based on a recent report that Fe in NiFe mixed hydroxides can possibly prevent further oxidation from Ni^{2+} to $Ni^{3+/4+}$ during the OER, thus improving the OER activity.[37,38] The surface morphology, chemical composition, and crystal structure of NiFe electroplated onto EP Ni–cotton were characterized by FE-SEM, XPS, and XRD measurements, respectively. As shown in **Figure 5**a,b, the NiFe layer was highly uniform. Additionally, the thickness and the loading mass of the EP NiFe layer was measured to be ≈460 nm (i.e., the total EP layer thickness of EP NiFe LDH/Ni was ≈1150 nm) and 8 mg cm^{-2}, respectively. The surface of the EP NiFe LDH electrode exhibited a hierarchical, wrinkled nanostructure while maintaining a highly porous 3D cellulose network without any blocking of the pores by NiFe. The Ni and Fe in NiFe mainly existed in the form of Ni^{2+} and Fe^{2+} (with some as Fe^{3+}), respectively (Figure 5c,d).[36,39] Moreover, the XRD pattern of NiFe exhibited additional (003), (006), and (009) peaks, which were assigned to NiFe LDH (Figure S21, Supporting Information).[39] The sheet resistance of the EP NiFe-coated cotton was measured to be ≈0.02 Ω sq^{-1}, which is slightly lower than that of the EP Ni–cotton (0.05 Ω sq^{-1}).

The OER performance of NiFe electroplated onto EP Ni–cotton (EP NiFe LDH/Ni–cotton) was evaluated in 1 M KOH using a three-electrode cell and was compared with those of commercial Ni foam and EP Ni–cotton by finding the optimal plating conditions (Figure 5e and Figures S22 and S23, Supporting Information). The effect of the capacitive current on the catalytic activity (by Ni ion oxidation) of the EP NiFe LDH/Ni–cotton was minimized by calculating the average activity from the forward and reverse sweeps of the cyclic voltammetry curve (Figures S24 and S25, Supporting Information).[11] The overpotential of the EP NiFe LDH/Ni–cotton electrode was lower than those of commercial Ni foam and EP Ni–cotton. Particularly, it is worth noting that the overpotentials (i.e., ≈214 mV at 50 mA cm^{-2} and ≈228 mV at 100 mA cm^{-2}) of the EP NiFe LDH/Ni–cotton electrode were significantly reduced compared to those of Ni-based OER electrodes reported by other research groups (Table S2, Supporting Information).[11,12,37,39] We also confirmed that the LbL-assembled Au layer buried below the EP Ni layer showed negligible activity toward the OER (Figure S26, Supporting Information).

The EP NiFe LDH/Ni–cotton electrode exhibited fast OER kinetics with a small Tafel slope of 27 mV dec^{-1} (Table S2, Supporting Information). As shown in Figure 5f, the EIS results confirm the fast OER kinetics of the EP NiFe LDH/Ni–cotton electrode. The R_s and R_{ct} of the EP NiFe LDH/Ni–cotton were measured to be ≈7.8 (at 100 kHz) and 5.3 Ω cm^{-2}, respectively, which are lower than those of the EP Ni–cotton electrode (R_s = 13.5 and R_{ct} = 16.0 Ω cm^{-2}). Typically, the R_s value is determined by the sum of the resistance generated from each cell component (i.e., electrolyte, active material, and current collector) and the interfaces (mainly, active material/current collector).[42] As mentioned earlier, the formed EP NiFe LDH/Ni–cotton anode showed better electrical conductivity than the EP Ni-cotton, along with an extremely large surface area with unique nanostructures. This is consistent with a recent report by Trotochaud et al., who observed that when Fe ions were incorporated into a Ni hydroxide lattice, they could act as n-type dopants and consequently increase the electrical conductivity of the Ni hydroxide with the formation of a distinct structure (i.e., NiFe LDH).[40,42] Additionally, it has been reported that the high electrical conductivity of the active material is a critical factor in achieving higher catalytic activities, which results in low R_s values.[44,45] For example, the NiFe LDH nanoarrays with improved electrical conductivity by modulating the density of oxygen vacancies on the materials' surface showed improved catalytic activities with a marked reduction in R_s values despite no notable geometrical changes.[46]

In particular, very similar metal hydroxide composition and structure between NiFe LDH and EP Ni–cotton surface (i.e., $Ni(OH)_2$) allow for stable connection through strong interfacial interactions, enabling negligible contact resistance and fast charge transfer as well as stable performance retention.[47] Thus, the significant reduction of R_s value for EP NiFe LDH/Ni–cotton anode (Figure 5f) can be attributed to the synergistic effect of improved electrical conductivity and stable interface structure, which can be more prominent in OER where large anodic overpotential occurs due to complex four-electron reaction.[48,49]

On the other hand, the R_{ct} mainly arising at the active material/electrolyte interface is greatly influenced by the geometric property and surface chemistry of the electrode.[50] The hierarchical 3D nanostructure of the EP NiFe LDH/Ni–cotton provides an extremely large active surface area with a number of exposed, highly active edge sites, which enables fast charge transfer (i.e., low R_{ct}) at all electrode/electrolyte interfaces. Moreover, this open 3D structure allows excellent electrolyte accessibility, which is highly advantageous in ion diffusion and gas release, resulting in superior electrocatalytic activity and stability. Based on these facts, the reduced resistances can be attributed to the improved charge transfer characteristics between the electrode (i.e., EP NiFe LDH/Ni–cotton) and the OER electrolyte based on the increased electrical conductivity and surface area (due to the formation of wrinkled nanostructures, as shown in Figure 5a, which was enabled by the additional NiFe electroplating). We also confirmed that our OER electrode did not have any carbon corrosion phenomenon (i.e., the generation of CO_2 gas as a byproduct) despite the use of cotton textile because the applied current was

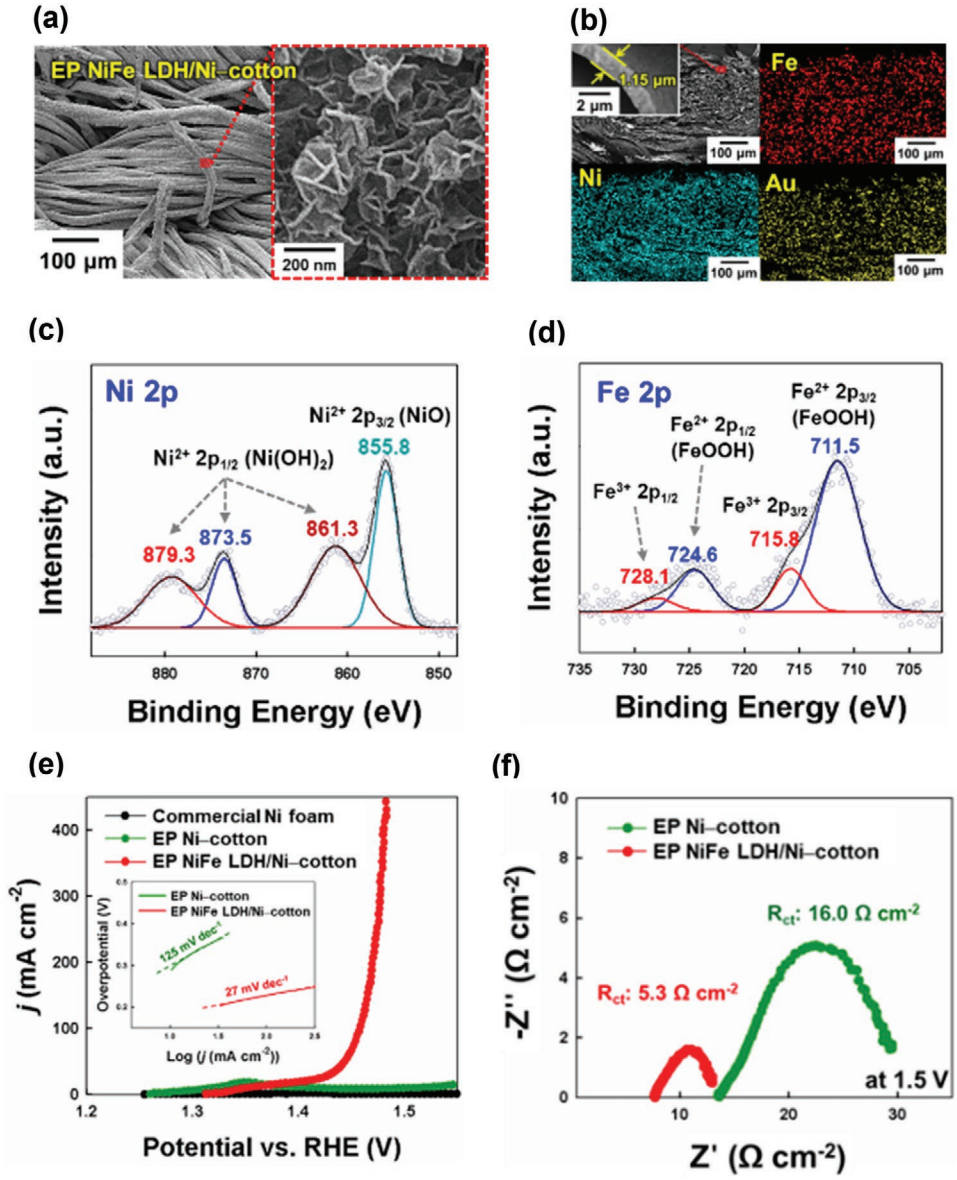

Figure 5. a) Planar FE-SEM images and b) cross-sectional FE-SEM and EDX mapping images of the EP NiFe LDH/Ni–cotton electrode (the top left inset shows the thickness of the NiFe LDH/Ni layer). XPS spectra of c) Ni 2p and d) Fe 2p for the EP NiFe LDH/Ni–cotton electrode. e) OER polarization curves for Ni foam, EP Ni–cotton, and EP NiFe LDH/Ni–cotton electrodes in a 1 M KOH electrolyte at a scan rate of 1 mV s^{-1} (the inset shows the Tafel plot). f) EIS plots for the EP Ni–cotton and EP NiFe LDH/Ni–cotton electrodes recorded at an applied potential of 1.5 V versus RHE.

exclusively around the highly conductive metal layer coated onto the cotton textile (Figure S27, Supporting Information).

To assess the long-term stability of our OER electrode, we conducted an accelerated durability test in 1 M KOH electrolyte by repeating potential sweeps up to 10 000 cycles. The EP NiFe LDH/Ni–cotton electrode exhibited good operation durability with only a negligible drop in current density after 10 000 cycles. We also evaluated the catalytic durability of EP NiFe LDH/Ni–cotton using a chronopotentiometry test at 10 and 50 mA cm^{-2} for 24 h. As shown in Figure S28, Supporting Information, the potential was maintained with minimal decay during the chronopotentiometry test for 24 h, demonstrating the good stability of the electrode in the alkaline OER. Additionally, the EP NiFe LDH/Ni–cotton electrode maintained high OER performance even at mechanically folded states (Figure S29, Supporting Information). In the case of folding the electrode one and two times, 93.6% and 92.2% of the initial OER current were maintained. These results evidently show that our electroplated electrodes are also mechanically stable, and furthermore can meet the flexibility demands.

2.4. Two-Electrode Water Electrolyzer Using HER and OER Textile Electrodes

To investigate the overall water-splitting performance, we prepared a full-cell device composed of EP Ni–cotton (the cathode

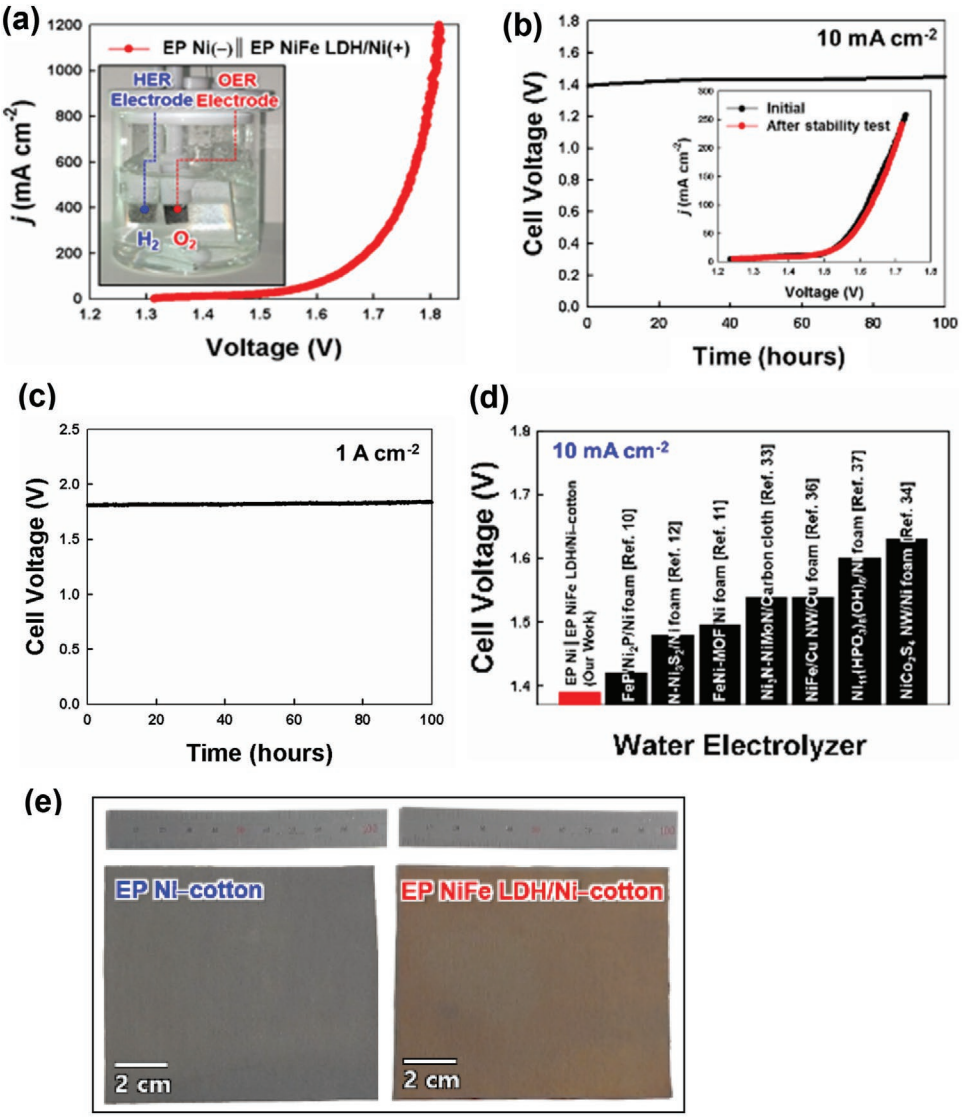

Figure 6. a) Photograph and polarization curve of the EP Ni–cotton‖EP NiFe LDH/Ni–cotton electrodes (the inset photograph shows the generation of hydrogen and oxygen gas in the HER and OER electrodes, respectively). b) Chronopotentiometry curve of the EP Ni–cotton‖EP NiFe LDH/Ni–cotton electrode recorded at 10 mA cm^{-2}. The inset shows the polarization curves before and after the stability test (inset) for the EP Ni–cotton‖EP NiFe LDH/Ni–cotton electrodes. c) Chronopotentiometry curve of the EP Ni–cotton‖EP NiFe LDH/Ni–cotton electrode recorded at 1 A cm^{-2}. d) Comparison of the cell voltages (at 10 mA cm^{-2}) between the EP Ni–cotton‖EP NiFe LDH/Ni–cotton electrodes (in our work) and other non-noble metal-based water-splitting electrodes (reported by other research groups). e) Photograph of the large-scale EP Ni–cotton and EP NiFe LDH/Ni–cotton electrodes.

for the HER) and EP NiFe LDH/Ni–cotton (the anode for the OER) (**Figure 6**a and Figure S30, Supporting Information). In this case, the cell voltages of the EP Ni‖EP NiFe LDH/Ni–cotton cell were measured to be ≈1.39, 1.63, and 1.81 V at 10, 100, and 1000 mA cm^{-2}, respectively (Figure 6a and Table S3, Supporting Information), which was much lower than those of Pt/C and IrO_2 catalyst-loaded Ni foams (i.e., Pt/C/Ni foam (–) ‖ IrO_2/Ni foam (+), 1.55 V at 10 mA cm^{-2}, 1.67 V at 100 mA cm^{-2}) (Figure S31, Supporting Information). When the operational stability of the EP Ni‖EP NiFe LDH/Ni–cotton cell was evaluated by chronopotentiometry at a current density of 10 mA cm^{-2} for 100 h in 1 M KOH (Figure 6b), the cell voltage remained constant at ≈1.4 V. The polarization curve after chronopotentiometry for 100 h was nearly identical to the initial curve. We also confirmed that the operational stability of our device could be well maintained even at an extremely high current density of 1 A cm^{-2} for 100 h in 1 M KOH (Figure 6c). Furthermore, after such a harsh durability test, the EP NiFe LDH/Ni–cotton electrode did not exhibit the physical and chemical degradations such as delamination and crack of the electroplated layer as well as leakage of Ni and Fe ions (Figure S32, Supporting Information). These results indicate the excellent stability of our full-cell device against the long-term operation of water electrolysis. Particularly, from the polarization curves of water electrolysis in 1 M KOH, the full cell exhibited an extremely low cell voltage of 1.39 V

at 10 mA cm^{-2}, which is superior to (i.e., lower than) those of conventional non-noble metal-based full-cell devices under the same experimental conditions (Figure 6d).

Futhermore, when the experimentally measured amount of the generated H_2 and O_2 gases was compared with the amount of theoretical products (calculated from the amount of charge passed at different time intervals), the faradaic efficiency was estimated to be ≈99.7% (Figure S33, Supporting Information). We attribute this excellent performance to the extremely large surface area of the highly porous cotton-based electrodes with metal-like conductivity, the crystalline structure of nickel oxides, and the facile charge transport. As a result, our approach is highly effective for preparing large-scale HER and OER electrodes because the LbL-assembly of metal NPs and commercial two-electrode-based electroplating can be easily carried out irrespective of substrate size and shape (Figure 6e). In addition to the effectiveness of the cotton-based electrodes, we highlight that TOA-Ag NPs and TOA-Cu NPs as well as TOA-Au NPs can be used for the preparation of EP Ni–cotton and EP NiFe LDH–cotton electrodes using the same abovementioned approach and experimental conditions (Figures S34–S40, Supporting Information). Furthermore, it should be noted that our approach can be easily applied to various flexible and porous substrates, such as polyester, paper or nylon (Figures S41 and S42, Supporting Information).

3. Conclusion

Using highly porous cotton textile electrodes fabricated by a LbL-assembled metal NP-driven electroplating approach, we demonstrated that our textile electrodes could exhibit considerably high HER and OER performances. Our NP assembly approach completely converted insulating cotton to a highly conductive textile while preserving its porosity and large surface area. Additionally, the metal NP-assembled cotton fibrils induced the uniform electroplating of electrocatalytic Ni and NiFe without any metal agglomeration. This capability to control the interfacial structure between conductive and catalytic phases enabled the considerably low overpotentials and fast reaction kinetics of EP Ni–cotton for the HER (i.e., 12 mV at 10 mA cm^{-2} and 32.7 mV dec^{-1}) and EP NiFe LDH/Ni–cotton for the OER (i.e., 214 mV at 50 mA cm^{-2} and 27 mV dec^{-1}). For the full-cell device combining EP Ni–cotton and EP NiFe LDH/Ni–cotton electrodes, the cell voltage was measured to be 1.39 V at 10 mA cm^{-2}. Furthermore, our full cell device exhibited stable operation at an extremely high current density of 1 A cm^{-2} for at least 100 h in 1 M KOH. Given that our approach can be applied to other porous substrates irrespective of substrate size or shape, we believe that this strategy can provide a basis for designing other high-performance electrochemical electrodes (i.e., lithium-ion batteries, supercapacitors, and biofuel cells) and water-splitting electrodes that require a large active surface area and facile charge transport.

4. Experimental Section

Synthesis of TOA-Au NPs: Tetraoctylammonium bromide-stabilized Au NPs (TOA-Au NPs) in toluene were prepared according to the Brust–Schiffrin method.[51] In brief, 25×10^{-3} M tetraoctylammonium bromide dissolved in toluene (80 mL) and 30×10^{-3} M $HAuCl_4$ dissolved in deionized water (30 mL) were mixed under stirring. Then, a freshly prepared 0.4 M $NaBH_4$ solution (25 mL) was added to the mixture and immediately reduced. After 30 min of reaction, the toluene phase was washed with 0.1 M H_2SO_4, 0.1 M NaOH, and deionized water (3 times).

Synthesis of TOA-Ag NPs: Tetraoctylammonium thiosulfate-stabilized Ag NPs (TOA-Ag NPs) with a diameter of ≈7 nm in toluene were prepared by the modified Brust–Schiffrin method.[51] In brief, 2.25×10^{-3} M tetraoctylammonium bromide was dissolved in toluene (24 mL), and 0.9×10^{-3} M silver nitrate was dissolved in deionized water (24 mL) with 3.6×10^{-3} M sodium thiosulfate and stirred. Then, a freshly prepared 1.35×10^{-3} M $NaBH_4$ solution (24 mL) was added to the mixture and immediately reduced. After 10 min of reaction, the toluene phase was washed with 0.01 M HCl, 0.01 M NH_4OH, and deionized water (3 times).

Synthesis of TOA-Cu NPs: Tetraoctylammonium thiosulfate-stabilized Cu NPs (TOA-Cu NPs) with a size of ≈7.5 nm in toluene were prepared by the modified Brust–Schiffrin method.[51] In brief, 0.75×10^{-3} M tetraoctylammonium bromide was dissolved in toluene (8 mL), and 0.3×10^{-3} M copper (II) chloride dihydrate was dissolved in deionized water (7 mL) with 1.2×10^{-3} M sodium thiosulfate and stirred. Then, a freshly prepared 0.9×10^{-3} M $NaBH_4$ solution (1 mL) was added to the mixture and immediately reduced. After 10 min of reaction, the toluene phase was washed three times with 0.01 M HCl, 0.01 M NH_4OH, and deionized water.

Preparation of (TOA-Au, -Ag, or -Cu NP/DETA)$_n$-Coated Cotton: First, a PEI solution (2 mg mL^{-1}, $M_w \approx 800$ g mol^{-1}) was dissolved in ethanol and adsorbed onto the substrate. After washing the PEI-coated cotton with pure ethanol, the 15 mg mL^{-1} TOA-Au NP solution was sequentially deposited on the PEI-coated cotton. This procedure was followed by washing the cotton with pure toluene to remove the weakly adsorbed TOA-Au NPs (or TOA-Ag NPs) on the PEI-coated substrate, and then the outermost TOA ligand layer was replaced with the DETA (2 mg mL^{-1}) linker in ethanol. After this ligand-exchange reaction, the weakly adsorbed DETA layer was likewise washed three times with pure ethanol. This deposition cycle was repeated until the desired number of bilayers was reached. Additionally, the (TOA-Ag NP/DETA)$_n$-coated cotton was prepared using the same abovementioned procedures. When preparing the TOA-Cu NP-coated cotton, cysteamine molecules were used as organic linkers (i.e., (TOA-Cu NP/cysteamine)$_n$-coated cotton) instead of DETA because the DETA linker solution dissolves the Cu NPs. The concentration of cysteamine in ethanol was fixed at 2 mg mL^{-1}. Additionally, all the experimental procedures for depositing TOA-Cu NPs and cysteamine onto the cotton substrates were identical to those of (TOA-Au NP/DETA)$_n$-coated cotton substrates.

Preparation of EP Ni–Cotton: The as-prepared (TOA-Au NP/DETA)$_4$-coated cotton was immersed in a typical Watt bath (240 g L^{-1} $NiSO_4$, 45 g L^{-1} $NiCl_2$, and 30 g L^{-1} H_3BO_3).[52] The process of Ni electroplating based on a two-electrode system was performed on (TOA-Au NP/DETA)$_4$-coated cotton as a cathode and a Ni plate as an anode. These procedures were also applied to (TOA-Ag NP/DETA)$_n$- or (TOA-Cu NP/cysteamine)$_n$-coated cotton. In this case, the separation distance between the cathode and anode was fixed at 2 cm. Then, an external current density of 346 mA cm^{-2} was applied to the sample for 30 min at room temperature, and the sample was washed three times in deionized water and dried at room temperature (Ni loading amount: 0.0522 g cm^{-2}). These EP Ni–cotton electrodes were dipped into a 0.1 M KOH solution for 60 min for the additional formation of $Ni(OH)_2$, washed in deionized water and dried at room temperature.

When preparing EP Ni–cotton using TOA-Ag NPs or TOA-Cu NPs instead of TOA-Au NPs, the sheet resistances of (TOA-Ag NP/DETA)$_n$- or (TOA-Cu NP/cysteamine)$_n$-coated cotton were first adjusted below 1000 Ω sq^{-1} with increasing bilayer number (n). After lowering the sheet resistances, Ni electroplating was carried out on (TOA-Ag NP/DETA)$_n$- or (TOA-Cu NP/cysteamine)$_n$-coated cotton.

Preparation of EL Ni–Cotton: The EL Ni deposition on cotton followed the reported procedure.[53] Briefly, cellulose cotton was first immersed into a sensitizing solution (0.05 M $SnCl_2 \cdot 2H_2O$ and 0.15 M HCl) and a $PdCl_2$ solution (0.6×10^{-3} M $PdCl_2$ and 0.03 M HCl). After the substrate

was washed three times with deionized water, 45 g L^{-1} $NiSO_4 \cdot 6H_2O$, 240 g L^{-1} $NaH_2PO_2 \cdot H_2O$, 30 g L^{-1} $NaC_6H_5O_7 \cdot 2H_2O$ and 50 g L^{-1} NH_4Cl were added to the mixture, which was stirred at room temperature and adjusted to pH 9 using NH_4OH. After increasing the temperature of the solution to 80 °C, the cotton substrate was inserted, and the mixture was stirred for 120 min. After the reaction, the electrodes were repeatedly washed with deionized water and dried. After the chemical reduction process, these EL Ni–cotton electrodes were dipped into a 0.1 M KOH solution for 60 min for the additional formation of $Ni(OH)_2$, washed in deionized water and dried at room temperature. In particular, this oxidation process using KOH solution was applied to all the samples, including the EP Ni–cotton, porous Ni foam, Ni plate and EL Ni–cotton, under the same experimental conditions.

Preparation of EP NiFe LDH/Ni–Cotton: The EP NiFe LDH deposition on cotton followed the reported procedure with slight modifications.[54] NiFe LDH was deposited on a prepared EP Ni–cotton electrode from an aqueous electrolyte bath containing 3×10^{-3} M $Ni(NO_3)_2 \cdot 6H_2O$ and 3×10^{-3} M $Fe(NO_3)_3 \cdot 9H_2O$. Electrodeposition was carried out in a potentiometric manner in a two-electrode configuration consisting of EP Ni–cotton as the anode and a Ni plate as the cathode. The potential was held constant at −2.5 V for 60 min. After electrodeposition, the electrode was carefully removed, washed several times with deionized water and dried.

Preparation of Pt/C/Ni Foam: Pt/C/Ni foam catalysts were prepared by dispersing 1 mg Pt/C (20 wt% Pt on Vulcan XC-72) in 300 µL of EtOH solution containing 10.5 µL of 5 wt% Nafion.[55] This catalyst ink solution was deposited onto the commercial Ni foam (0.5×0.5 cm^2), and then dried at room temperature.

Preparation of IrO_2/Ni Foam: IrO_2/Ni foam catalysts were prepared by dispersing 1 mg IrO_2 in 300 µL of EtOH solution with 10.5 µL of 5 wt% Nafion.[55] As already mentioned above, this catalyst ink solution was loaded onto the commercial Ni foam (0.5×0.5 cm^2), and then dried at room temperature.

Characterization: The crystal structure and size distribution of TOA-Au NPs were examined by high-resolution transmission electron microscopy (HR-TEM) (Tecnai 20, FEI). The XPS spectra of the electrodes were investigated using XPS (X-TOOL, ULVAC-PHI) with Al Kα radiation. The crystallinity of the EP Ni–cotton, EL Ni–cotton and EP NiFe LDH/Ni–cotton surfaces was analyzed with their X-ray diffraction (XRD) patterns obtained from SmartLab (Rigaku) with Cu Kα radiation. To determine the absorption mechanism during the ligand-exchange reaction, the FTIR spectra of the multilayer films were measured with a Cary 600 spectrometer (Agilent Technology) operated at a 4 cm^{-1} resolution in attenuated total reflectance (ATR) mode. The raw data were plotted after baseline correction and smoothing using spectral analysis software (Omnic 9, Thermo Scientific). SEM and energy-dispersive X-ray (EDX) spectroscopy images were observed via FE-SEM (Quanta 250 FEG, FEI). The Brunauer–Emmett–Teller (BET) specific surface areas of the EP Ni–cotton, EL Ni–cotton, and Au NP coated–cotton were measured using N_2 (99.999%) adsorption at 77 K (BELSORP-mini II, MicrotracBEL, Corp). The specific surface of bare cotton was determined using mercury intrusion porosimetry (MicroActive AutoPore V9600) that could operate in the interval 0.20–33 000 psi to estimate the cores between 0.006 and 800 µm.

Molecular Dynamics Simulations: All-atom MD simulations were performed for a model system consisting of DETA molecules between Au (100) surfaces. The initial molecular geometries were prepared by placing *n* DETA molecules between Au slabs built by FCC stacking with a (100) face consisting of a 7×7 supercell. With this system configuration, NPT-ensemble MD simulations were carried out at 298 K and 1 bar using the Forcite module with COMPASS force field[56] (COMPASS II), as implemented in the Material Studio package. The Nose-Hoover-Langevin thermostat[57] and Parrinello-Rahman barostat[58] were used to maintain the temperature (298 K) and pressure (1 bar). For all NPT MD runs, the electrostatic potential energy was calculated by the Ewald summation method with an accuracy of 0.1 kcal mol^{-1} and a buffer width of 0.5 Å. The van der Waals potential energy was calculated by the atom-based technique with a cutoff distance of 12.5 Å and a spline width of 1 Å. The MD system was equilibrated for 5 ns with a time step of 1 fs.

Electrochemical Characterization: All electrochemical measurements, including polarization curves, cyclic voltammetry, and EIS, were carried out with an Ivium-n-Stat electrochemical workstation (Ivium Technologies). For measurements in the three-electrode cell system, a Pt mesh and an RHE were used as the counter and reference electrodes, respectively, while using 1 M KOH (pH = 14) as the electrolyte. The OER and HER catalytic activities were measured by linear sweep voltammetry at scan rates of 1 and 10 mV s^{-1}, respectively, with iR compensation. All reported current densities were based on the geometric surface area of the electrodes. The EIS measurements were performed with a biased working electrode over a frequency range from 100 kHz to 0.01 Hz and potentials of 1.5 V (vs RHE) for the OER and −0.1 V (vs RHE) for the HER, respectively. Thus, the semicircle diameter corresponds to the charge transfer resistance (R_{ct}), which can be used to evaluate the charge transfer kinetics on the surface of the electrode. The starting point on the *x*-axis of the semicircle represents the series resistance, which is the sum of the ionic resistance of the electrolyte, the intrinsic resistance of the active materials and the contact resistance at the active material/current collector interface.

For carbon corrosion tests (in situ gas analysis) of OER electrodes, a mass spectrometer (Cirrus 2, MKS Instruments) was connected to the electrochemical cell in series. Ar gas (ultrahigh purity, Airgas) was fed into the electrochemical cell as a carrier gas (flow rate of 20 mL min^{-1}) controlled by a mass flow controller (G-series, MKS Instruments).

Inductively coupled plasma optical emission spectrometry (ICP-OES, Agilent Technologies 5900, VistaChipII CCD detector) was performed to detect the amount of Ni and Fe ions dissolved in the electrolyte after stability testing at the current density of 1 A cm^{-2}.

The faradaic efficiency of water splitting was measured by the eudiometry method in the experimental setups. The working electrode was fixed at the inside of an inverted burette filled with the electrolyte. All the metal wires connecting the working electrode were coated with insulating epoxy to prevent a loss of charge from side reactions. The evolved gases were directly collected in the headspace of the inverted burette, and the corresponding gas volume was determined by the displacement of the vertical water column. Based on this method, the faradaic efficiency was calculated by comparing the amount of evolved gas with the theoretical amount of gas, which is calculated by the charge passed through the electrode:

$$\text{Faradaic efficiency}(H_2) = \frac{V_{\text{experiment}}}{V_{\text{theoretical}}} = \frac{V_{\text{experiment}}}{\frac{2}{4} \times \frac{Q}{F} \times V_m} \quad (1)$$

$$\text{Faradaic efficiency}(O_2) = \frac{V_{\text{experiment}}}{V_{\text{theoretical}}} = \frac{V_{\text{experiment}}}{\frac{1}{4} \times \frac{Q}{F} \times V_m} \quad (2)$$

where *F* is the Faraday constant (96 485 C mol^{-1}), *Q* is the summation of the charge passed through the electrodes, the number 4 indicates 4 moles of electrons per mole of H_2O, the number 2 indicates 2 moles of H_2 per mole of H_2O, the number 1 indicates 1 mole of O_2 per mole of H_2O and V_m is the molar volume of gas (24.5 L mol^{-1}, 298 K, 101 kPa).[59]

Supporting Information

Supporting Information is available from the Wiley Online Library or from the author.

Acknowledgements

This work was supported by a National Research Foundation of Korea (NRF) grant funded by the Korea government (NRF-2019R1A4A1027627, NRF-2019M3E6A1064711, and NRF-2021R1A2C3004151).

Conflict of Interest

The authors declare no conflict of interest.

Data Availability Statement

Research data are not shared.

Keywords

electrocatalytic fibrils, layer-by-layer assembly, water splitting reaction

Received: March 15, 2021
Revised: May 13, 2021
Published online: June 12, 2021

[1] R. Subbaraman, D. Tripkovic, D. Strmcnik, K.-C. Chang, M. Uchimura, A. P. Paulikas, V. Stamenkovic, N. M. Markovic, *Science* **2011**, *334*, 1256.
[2] X. Zou, Y. Zhang, *Chem. Soc. Rev.* **2015**, *44*, 5148.
[3] Y. Jiao, Y. Zheng, M. Jaroniec, S. Z. Qiao, *Chem. Soc. Rev.* **2015**, *44*, 2060.
[4] J. K. Nørskov, T. Bligaard, A. Logadottir, J. R. Kitchin, J. G. Chen, S. Pandelov, U. Stimming, *J. Electrochem. Soc.* **2005**, *152*, J23.
[5] N. Danilovic, R. Subbaraman, D. Strmcnik, K.-C. Chang, A. P. Paulikas, V. R. Stamenkovic, N. M. Markovic, *Angew. Chem., Int. Ed.* **2012**, *51*, 12495.
[6] D. Y. Chung, P. P. Lopes, P. Farinazzo Bergamo Dias Martins, H. He, T. Kawaguchi, P. Zapol, H. You, D. Tripkovic, D. Strmcnik, Y. Zhu, S. Seifert, S. Lee, V. R. Stamenkovic, N. M. Markovic, *Nat. Energy* **2020**, *5*, 222.
[7] R. Subbaraman, D. Tripkovic, K.-C. Chang, D. Strmcnik, A. P. Paulikas, P. Hirunsit, M. Chan, J. Greeley, V. Stamenkovic, N. M. Markovic, *Nat. Mater.* **2012**, *11*, 550.
[8] J. Mahmood, F. Li, S.-M. Jung, M. S. Okyay, I. Ahmad, S.-J. Kim, N. Park, H. Y. Jeong, J.-B. Baek, *Nat. Nanotechnol.* **2017**, *12*, 441.
[9] D.-Y. Wang, M. Gong, H.-L. Chou, C.-J. Pan, H.-A. Chen, Y. Wu, M.-C. Lin, M. Guan, J. Yang, C.-W. Chen, Y.-L. Wang, B.-J. Hwang, C.-C. Chen, H. Dai, *J. Am. Chem. Soc.* **2015**, *137*, 1587.
[10] F. Yu, H. Zhou, Y. Huang, J. Sun, F. Qin, J. Bao, W. A. Goddard, S. Chen, Z. Ren, *Nat. Commun.* **2018**, *9*, 2551.
[11] D. Senthil Raja, H.-W. Lin, S.-Y. Lu, *Nano Energy* **2019**, *57*, 1.
[12] P. Chen, T. Zhou, M. Zhang, Y. Tong, C. Zhong, N. Zhang, L. Zhang, C. Wu, Y. Xie, *Adv. Mater.* **2017**, *29*, 1701584.
[13] H. Zhou, F. Yu, Q. Zhu, J. Sun, F. Qin, L. Yu, J. Bao, Y. Yu, S. Chen, Z. Ren, *Energy Environ. Sci.* **2018**, *11*, 2858.
[14] L.-L. Feng, G. Yu, Y. Wu, G.-D. Li, H. Li, Y. Sun, T. Asefa, W. Chen, X. Zou, *J. Am. Chem. Soc.* **2015**, *137*, 14023.
[15] J. Yang, X. Wang, B. Li, L. Ma, L. Shi, Y. Xiong, H. Xu, *Adv. Funct. Mater.* **2017**, *27*, 1606497.
[16] B. Yao, J. Zhang, T. Kou, Y. Song, T. Liu, Y. Li, *Adv. Sci.* **2017**, *4*, 1700107.
[17] M. Park, Y. Kim, Y. Ko, S. Cheong, S. W. Ryu, J. Cho, *J. Am. Chem. Soc.* **2014**, *136*, 17213.
[18] L. Peng, X. Peng, B. Liu, C. Wu, Y. Xie, G. Yu, *Nano Lett.* **2013**, *13*, 2151.
[19] S. W. Lee, N. Yabuuchi, B. M. Gallant, S. Chen, B.-S. Kim, P. T. Hammond, Y. Shao-Horn, *Nat. Nanotechnol.* **2010**, *5*, 531.
[20] B. A. Korgel, S. Fullam, S. Connolly, D. Fitzmaurice, *J. Phys. Chem. B* **1998**, *102*, 8379.
[21] Y. Kim, J. Zhu, B. Yeom, M. Di Prima, X. Su, J.-G. Kim, S. J. Yoo, C. Uher, N. A. Kotov, *Nature* **2013**, *500*, 59.
[22] M. Gao, W. Sheng, Z. Zhuang, Q. Fang, S. Gu, J. Jiang, Y. Yan, *J. Am. Chem. Soc.* **2014**, *136*, 7077.
[23] A. K. Shukla, S. Venugopalan, B. Hariprakash, *J. Power Sources* **2001**, *100*, 125.
[24] G. A. Snook, N. W. Duffy, A. G. Pandolfo, *J. Power Sources* **2007**, *168*, 513.
[25] J. Tizfahm, B. Safibonab, M. Aghazadeh, A. Majdabadi, B. Sabour, S. Dalvand, *Colloids Surf., A* **2014**, *443*, 544.
[26] D. S. Hall, D. J. Lockwood, C. Bock, B. R. MacDougall, *Proc. R. Soc. A* **2015**, *471*, 20140792.
[27] Z. Zeng, K.-C. Chang, J. Kubal, N. M. Markovic, J. Greeley, *Nat. Energy* **2017**, *2*, 17070.
[28] X. Yu, J. Zhao, L.-R. Zheng, Y. Tong, M. Zhang, G. Xu, C. Li, J. Ma, G. Shi, *ACS Energy Lett.* **2018**, *3*, 237.
[29] S. St John, R. W. Atkinson, R. R. Unocic, T. A. Zawodzinski, A. B. Papandrew, *J. Phys. Chem. C* **2015**, *119*, 13481.
[30] J. Durst, A. Siebel, C. Simon, F. Hasché, J. Herranz, H. A. Gasteiger, *Energy Environ. Sci.* **2014**, *7*, 2255.
[31] R. Kavian, S.-I. Choi, J. Park, T. Liu, H.-C. Peng, N. Lu, J. Wang, M. J. Kim, Y. Xia, S. W. Lee, *J. Mater. Chem. A* **2016**, *4*, 12392.
[32] S. Sirisomboonchai, S. Li, A. Yoshida, S. Kongparakul, C. Samart, Y. Kansha, X. Hao, A. Abudula, G. Guan, *Catal. Sci. Technol.* **2019**, *9*, 4651.
[33] A. Wu, Y. Xie, H. Ma, C. Tian, Y. Gu, H. Yan, X. Zhang, G. Yang, H. Fu, *Nano Energy* **2018**, *44*, 353.
[34] A. Sivanantham, P. Ganesan, S. Shanmugam, *Adv. Funct. Mater.* **2016**, *26*, 4661.
[35] X. Su, X. Li, C. Y. A. Ong, T. S. Herng, Y. Wang, E. Peng, J. Ding, *Adv. Sci.* **2019**, *6*, 1801670.
[36] L. Yu, H. Zhou, J. Sun, F. Qin, F. Yu, J. Bao, Y. Yu, S. Chen, Z. Ren, *Energy Environ. Sci.* **2017**, *10*, 1820.
[37] P. W. Menezes, C. Panda, S. Loos, F. Bunschei-Bruns, C. Walter, M. Schwarze, X. Deng, H. Dau, M. Driess, *Energy Environ. Sci.* **2018**, *11*, 1287.
[38] G.-F. Chen, T. Y. Ma, Z.-Q. Liu, N. Li, Y.-Z. Su, K. Davey, S.-Z. Qiao, *Adv. Funct. Mater.* **2016**, *26*, 3314.
[39] L. Ma, Y. Hu, R. Chen, G. Zhu, T. Chen, H. Lv, Y. Wang, J. Liang, H. Liu, C. Yan, H. Zhu, Z. Tie, Z. Jin, J. Liu, *Nano Energy* **2016**, *24*, 139.
[40] L. Trotochaud, S. L. Young, J. K. Ranney, S. W. Boettcher, *J. Am. Chem. Soc.* **2014**, *136*, 6744.
[41] F. Song, L. Bai, A. Moysiadou, S. Lee, C. Hu, L. Liardet, X. Hu, *J. Am. Chem. Soc.* **2018**, *140*, 7748.
[42] Z. He, F. Mansfeld, *Energy Environ. Sci.* **2009**, *2*, 215.
[43] S. Klaus, Y. Cai, M. W. Louie, L. Trotochaud, A. T. Bell, *J. Phys. Chem. C* **2015**, *119*, 7243.
[44] R. Fan, Q. Mu, Z. Wei, Y. Peng, M. Shen, *J. Mater. Chem. A* **2020**, *8*, 9871.
[45] A. Karmakar, K. Karthick, S. S. Sankar, S. Kumaravel, R. Madhu, S. Kundu, *J. Mater. Chem. A* **2021**, *9*, 1314.
[46] Z. Yuan, S.-M. Bak, P. Li, Y. Jia, L. Zheng, Y. Zhou, L. Bai, E. Hu, X.-Q. Yang, Z. Cai, Y. Sun, X. Sun, *ACS Energy Lett.* **2019**, *4*, 1412.
[47] S. Sirisomboonchai, S. Li, A. Yoshida, X. Li, C. Samart, A. Abudula, G. Guan, *ACS Sustainable Chem. Eng.* **2019**, *7*, 2327.
[48] L. Ji, H.-Y. Hsu, X. Li, K. Huang, Y. Zhang, J. C. Lee, A. J. Bard, E. T. Yu, *Nat. Mater.* **2017**, *16*, 127.
[49] E. Fabbri, T. J. Schmidt, *ACS Catal.* **2018**, *8*, 9765.
[50] H. Zhang, X. Li, A. Hähnel, V. Naumann, C. Lin, S. Azimi, S. L. Schweizer, A. W. Maijenburg, R. B. Wehrspohn, *Adv. Funct. Mater.* **2018**, *28*, 1706847.
[51] M. Brust, M. Walker, D. Bethell, D. J. Schiffrin, R. Whyman, *J. Chem. Soc., Chem. Commun.* **1994**, 801.
[52] O. P. Watts, *Trans. Am. Electrochem. Soc.* **1916**, *29*, 395.

[53] S.-S. Tzeng, F.-Y. Chang, *Thin Solid Films* **2001**, *388*, 143.
[54] X. Lu, C. Zhao, *Nat. Commun.* **2015**, *6*, 6616.
[55] J. Yin, Y. Li, F. Lv, Q. Fan, Y.-Q. Zhao, Q. Zhang, W. Wang, F. Cheng, P. Xi, S. Guo, *ACS Nano* **2017**, *11*, 2275.
[56] H. Sun, *J. Phys. Chem. B* **1998**, *102*, 7338.
[57] A. A. Samoletov, C. P. Dettmann, M. A. J. Chaplain, *J. Stat. Phys.* **2007**, *128*, 1321.
[58] M. Parrinello, A. Rahman, *J. Appl. Phys.* **1981**, *52*, 7182.
[59] S. Zhao, J. Huang, Y. Liu, J. Shen, H. Wang, X. Yang, Y. Zhu, C. Li, *J. Mater. Chem. A* **2017**, *5*, 4207.